OPEN GEOMECHANICS

Effects of Particle Shape on the Shear Wave Velocity and Shear Modulus of 3D Printed Sand Analogs

Sheikh Sharif Ahmed [a] ***& Alejandro Martinez*** [a]

[a] *Civil and Environmental Engineering, University of California Davis.*

Published
16th March 2022
https://doi.org/10.5802/ogeo.9

Edited by
Ivo Herle
Institute of Geotechnical Engineering
Technische Universität Dresden
Germany

Reviewed by
Marcos Arroyo
Dept. of Civil and Environmental Eng.
Geotechnical Division
UPC Barcelona
Spain

Torsten Wichtmann
Chair of Soil Mech., Foundation Eng. and Env. Geotechnics
Ruhr-Universität Bochum
Germany

Jean-Michel Pereira
Laboratoire Navier
Ecole des Ponts ParisTech
France

Correspondence
Alejandro Martinez
Civil and Environmental Engineering,
University of California Davis
USA
amart@ucdavis.edu

Abstract. Isolating the effects of individual particle properties (e.g. shape, size, mineralogy, surface roughness) on the mechanical behavior of naturally occurring coarse-grained soils is a significant challenge in experimental studies. This challenge can be addressed by recent advances in 3D printing technology which enable generation of artificial sand-sized particles with independent control over particle size and shape. In this study, bender element tests are conducted to examine the isolated effects of particle shape on the shear wave velocity and shear modulus of 3D printed sand analogs. The experimental results show that the shear wave velocity and shear modulus of the 3D printed sand specimens exhibit a relationship with mean effective stress that is in agreement to that reported for natural sands. The specimens composed of 3D printed sands with greater particle roundness and sphericity exhibit greater shear wave velocity and shear modulus for a given void ratio, relative density, and mean effective stress. The changes in shear wave velocity can be captured in terms of differences in individual particle shape parameters such as roundness and sphericity as well as combined particle shape parameters such as regularity. Regression analysis is used to develop relationships between shear wave velocity and particle shape parameters and void ratio, which are shown to be in agreement with previously-published relationships and to reliably predict the shear wave velocity of natural sands. The results presented herein highlight the usefulness of testing 3D printed soils to identify functional trends and dependencies between soil response parameters and intrinsic properties. However, this requires verification of the results against published trends and assessment of the possible effects of the differences in constituent material between the 3D printed and the natural soils.

Keywords. 3D printing, additive manufacturing, particle shape, shear wave velocity, sand

1. Introduction

Inherent particle properties such as shape, gradation, surface texture and constituent material stiffness control the global mechanical behavior of granular soils [Santamarina, 2003]. Extending the understanding of the effects of individual particle properties on the behavior of soils could aid in the advancement of constitutive models as well as in the increased efficiency and robustness of geotechnical site characterization and design methodologies. A number of previous investigations have examined the effects of different particle properties on the engineering properties of coarse-grained soils, such as friction angle [e.g. Altuhafi et al., 2016, Kirkpatrick, 1965, Marschi et al., 1972, Vangla and Latha, 2015, Wang et al., 2013, Xiao et al., 2019] and shear wave velocity (V_s) and small-strain modulus (G_{max}) [e.g. Altuhafi et al., 2016, Bartake and Singh, 2007, Bui, 2009, Chang and Ko, 1982, Cho et al., 2006, Dutta et al., 2020, Hussien and Karray, 2015, Iwasaki and Tatsuoka, 1977, Liu and Yang, 2018, Liu et al., 2021, Menq, 2003, Patel et al., 2009, Payan et al., 2016a,b, Senetakis et al., 2012, Sharifipour et al., 2004, Wichtmann and Triantafyllidis, 2009, Yang and Gu, 2013]. Regarding the small-strain behavior, some studies have reported increases in V_s with decreases in the mean particle size (D_{50}) [Bartake and Singh, 2007, Patel et al., 2009]. Conversely, other studies such as Iwasaki and Tatsuoka [1977], Wichtmann and Triantafyllidis [2009], and Yang and Gu [2013] observed no significant effect of D_{50} on V_s, whereas Chang and Ko [1982], Menq [2003], Sharifipour et al. [2004], Bui [2009], and Hussien and Karray [2015] reported an increase in V_s with increasing D_{50}. Regarding the effects of particle shape, Cho et al. [2006], Bui [2009], Patel et al. [2009], and Lee et al. [2017] reported an increase in V_s and G_{max} with increasing particle roundness. However, Altuhafi et al. [2016], Liu and Yang [2018], and Liu et al. [2021] observed a decrease in small strain stiffness with increasing particle roundness.

These conflicting observations highlight the significant challenges in isolating the effects of individual particle properties and state on the response of natural soils. For instance, V_s has been shown to depend on particle size, shape, surface roughness, mineralogy, and void ratio [e.g. Cho et al., 2006, Otsubo et al., 2015]. Also, different parameters have been used to characterize a given particle property, and it is often unclear which one better captures the aspects of the behavior that govern the property of interest. For example, particle shape can be characterized in terms of roundness, sphericity, and regulatity, and soil state can be captured in terms of the void ratio, relative density, and state parameter, where the latter two are defined in terms of a reference (i.e. extreme void ratios and critical state line, respectively). Despite the aforementioned challenges, several studies have used synthetic soils or natural soil mixtures to isolate the effect of individual particle properties on soil response [e.g. Xiao et al., 2019].

3D printing technology has advanced rapidly in the last decade, offering a solution for the individual control of particle properties. The current technological capabilities can be used to generate artificial soil analogs with independent control over particle size, shape, and gradation [e.g. Adamidis et al., 2020, Hanaor et al., 2016]. Recent studies used 3D printing technology to generate analog particles of different sizes and shapes, and showed that these analogs can successfully replicate the morphology of natural particles [e.g. Adamidis et al., 2020, Ahmed and Martinez, 2020, Athanassiadis et al., 2014, Hanaor et al., 2016, Miskin and Jaeger, 2013, Su et al., 2020]. Results of triaxial tests on 3D printed particles show that they exhibit stress-dilatancy behavior similar to that typical of natural soils [e.g. Adamidis et al., 2020, Ahmed and Martinez, 2021, Hanaor et al., 2016, Matsumura et al., 2017], and the interpretation of their mechanical response can be captured with the critical state soil mechanics framework [Ahmed and Martinez, 2021]. However, the 3D printed sands have a greater compressibility owing to the smaller stiffness of their polymeric constituent material. The V_s and G_{max} of 3D printed particles obtained by bender element tests have also shown a dependency on mean effective stress similar to that of natural sands [Ahmed and Martinez, 2020]. Other applications of 3D printed analogs include investigation of the frictional behavior of faults [Braun et al., 2021], effect of particle shape on clogging and discharge [Hafez et al., 2021], calibration of DEM simulations [Kittu et al., 2019, Peerun et al., 2021], permeability of uniformly graded soil [Adamidis et al., 2020, Wei et al., 2021], and development of transparent soil surrogates [Li et al., 2021]. These results highlight the usefulness of 3D printed synthetic soils as soil analogs that provide a high control over their properties. Further, the conclusions of some of these studies show that despite of the smaller stiffness of the 3D printed soils, they exhibit many of the similar behaviors and functional trends as natural soils.

The goal of this investigation is to examine the isolated effects of various particle shape parameters on the V_s and G_{max} of coarse-grained soils. To do so, seven 3D printed sands with different particle shape parameters but similar particle size distributions are first generated. Then, measurements of V_s and G_{max} are obtained in specimens composed of the 3D printed particles subjected to different magnitudes of isotropic confining effective stress. The trends obtained in this investigation are then compared to published relationships to assess consistency in the results.

2. Materials and Methods

2.1. 3D Printing Technology

Rapid advances in the 3D printing technology have developed different methods and materials in recent years. Modern 3D printers can be used to create complex objects using methods such as fused deposition modeling (FDM), stereolithography (SLA), digital light processing (DLP), and selective laser sintering (SLS) using polymeric, metallic, or ceramic materials, resulting in a wide range of precision and cost. While specialized 3D printers can mix materials on demand to achieve the desired mechanical properties and aesthetics to produce higly complex models [Jiménez

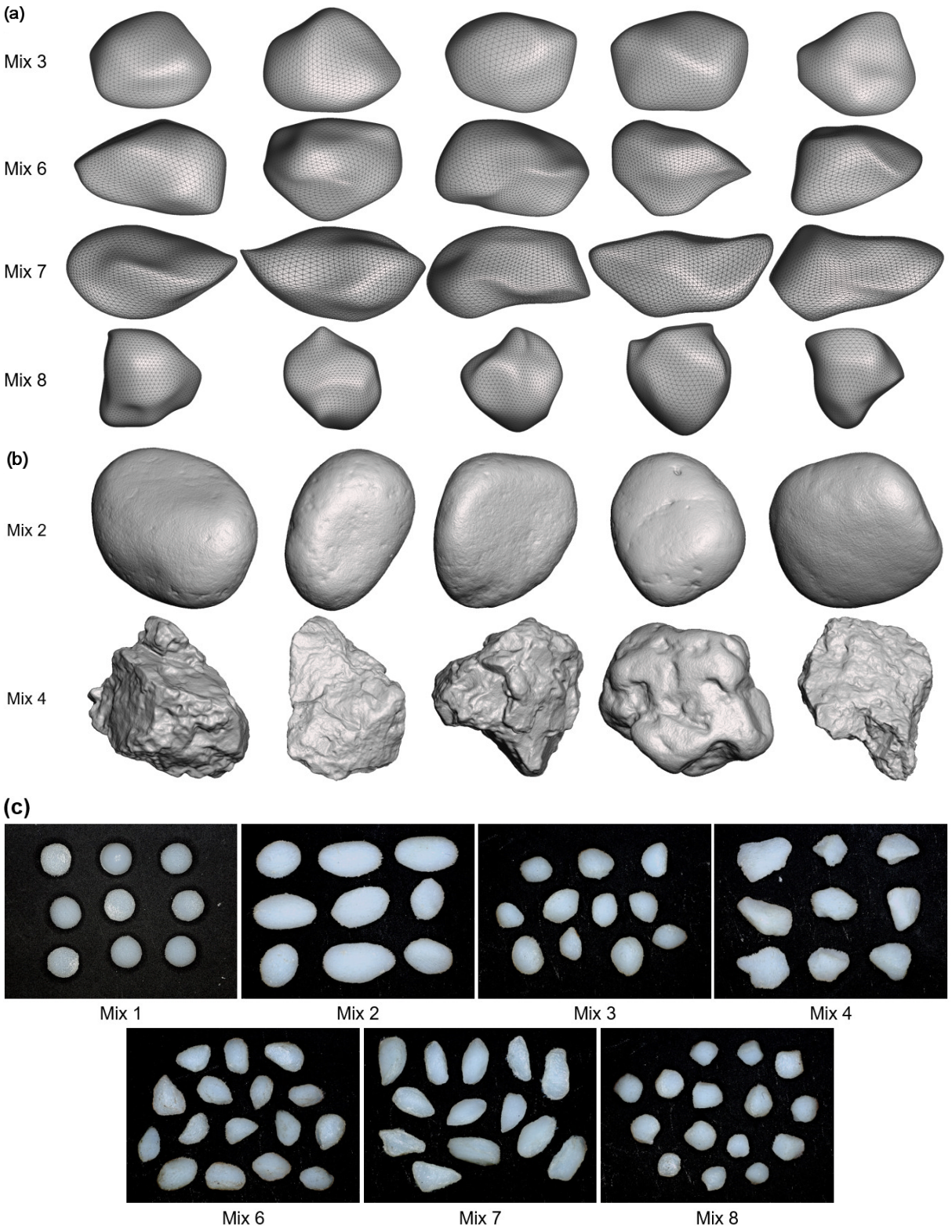

Figure 1. (a) 3D mesh of synthetic particles generated, (b) X-ray CT scans of mixes 2 and 4, and (c) 3D printed particles used in this study (not to scale). Note: mix 1 is composed of spheres; mixes 3, 6, 7 and 8 were created using spherical harmonics [after Wei et al., 2018]; and mixes 2 and 4 were generated from X-ray CT scans of rounded and angular sands, respectively.

et al., 2019, Najmon et al., 2019], typical desktop 3D printers are contrained to printing polymeric materials. These more economic printers typically print layers with a thickness as low as 10 μm and have a lateral resolution in the order of 20 to 40 μm [Ngo et al., 2018].

Table 1. Average and standard deviation (in parenthesis) of shape parameters of the 3D printed sand mixes

Soil specimen	Roundness, R	Circle ratio sphericity, S_C	Perimeter sphericity, S_P	Width-to-length ratio sphericity, S_{WL}	Convexity, C	Regularity, R_G [Cho et al., 2006]	Overall regularity, OR [Liu and Yang, 2018]	$SAGI$ [Altuhafi et al., 2016]
Mix 1	0.90 (0.09)	0.94 (0.01)	1.00 (0.00)	0.96 (0.02)	0.99 (0.00)	0.92 (0.05)	0.96 (0.02)	0.31 (0.30)
Mix 2	0.73 (0.09)	0.75 (0.10)	0.98 (0.02)	0.77 (0.11)	0.99 (0.00)	0.74 (0.08)	0.87 (0.04)	1.09 (0.99)
Mix 3	0.61 (0.12)	0.75 (0.04)	0.98 (0.01)	0.77 (0.04)	0.99 (0.00)	0.68 (0.07)	0.84 (0.04)	1.56 (0.57)
Mix 4	0.52 (0.13)	0.66 (0.10)	0.94 (0.03)	0.69 (0.13)	0.98 (0.01)	0.59 (0.08)	0.78 (0.05)	4.70 (1.93)
Mix 6	0.55 (0.13)	0.65 (0.05)	0.95 (0.01)	0.67 (0.06)	0.98 (0.01)	0.60 (0.07)	0.79 (0.04)	3.39 (1.23)
Mix 7	0.48 (0.12)	0.53 (0.04)	0.90 (0.02)	0.53 (0.04)	0.98 (0.01)	0.50 (0.06)	0.72 (0.03)	6.49 (1.96)
Mix 8	0.54 (0.11)	0.84 (0.04)	0.98 (0.01)	0.92 (0.05)	0.98 (0.00)	0.69 (0.07)	0.86 (0.03)	2.09 (0.95)

This study uses the polyjet 3D printing technology that offers relatively economical and fast manufacturing of small parts with high accuracy [Adamidis et al., 2020, Ahmed and Martinez, 2020, Kittu et al., 2019, Wei et al., 2021]. A polyjet printer has two print heads that deposit different liquid photopolymer resins. One resin generates the desired object while the other acts as the support structure, and both resins are hardened by ultraviolet laser. The layer thickness can be as low as 30 μm. Once the printing is completed, the support structure is removed by water jetting and chemical treatment using a 2% sodium hydroxide solution. Detailed description of the polyjet technology and its use to generate sand particles is provided in Ahmed and Martinez [2020, 2021].

2.2. 3D Printed Sands

The shape of a particle can be described by roundness and sphericity parameters, which can be defined in different ways [Guida et al., 2020, Mitchell et al., 2005]. This study considers the Wadell roundness (R) [Wadell, 1932], circle ratio sphericity (S_C), perimeter sphericity (S_P), width-to-length ratio sphericity (S_{WL}) and convexity (C) [Altuhafi et al., 2016, Mitchell et al., 2005], which are defined as:

$$R = \frac{\sum r_i / n}{R_{ins}} \tag{1}$$

$$S_C = \frac{D_{ins}}{D_{cir}} \tag{2}$$

$$S_P = \frac{P_C}{P_S} \tag{3}$$

$$S_{WL} = \frac{d_W}{d_L} \tag{4}$$

$$C = \frac{A_1}{A_1 + A_2} \tag{5}$$

where r_i is the radius of curvature of the edges or corners of a soil particle; n is the number of edges; R_{ins} is the radius of the maximum inscribed circle; D_{ins} is the diameter of the largest inscribing circle; D_{cir} is the diameter of the minimum circumscribing circle; P_C is the perimeter of a circle having the same projected area as the particle; P_S is the perimeter of the particle; d_W and d_L are width and length of a particle; and A_1 and $A_1 + A_2$ are the projected area and convex hull of a soil particle.

For this investigation, four materials were generated using the method proposed by Wei et al. [2018] that uses spherical harmonics to create random 3D shapes based on the desired shape features (mixes 3, 6, 7, and 8 in Figure 1a, Tables 1 and 2). These four materials were designed to have a D_{50} of 2.5 mm and a C_u of 1.26 (Table 2), R between 0.48 and 0.61, and S_C between 0.53 and 0.84. To extend the range of particle shape parameters considered in this investigation, the three 3D printed mixes used by Ahmed and Martinez [2020, 2021] were also tested. Two of these mixes (mix 2 and 4) were generated from the X-ray CT scans of randomly selected rounded and angular natural sand particles, respectively, as described by Ahmed and Martinez [2020] (Figure 1b, Tables 1 and 2). The D_{50} and C_u of these materials are 3.2 mm and 1.47, respectively. The last mix (mix 1) consisted of equal-sized spheres with a D_{50} of 3.2 mm and a C_u 1.0. These three mixes had greater R values (0.52 to 0.90) than the four mixes generated using spherical harmonics. Figure 2 shows the grain size distributions for all the soil mixes. Mixes 3, 6, 7 and 8 have identical grain size distributions with similar D_{50}, mixes 2 and 4 have a slightly larger D_{50}, and and the range of particle sizes in mix 1 is narrower. According to ASTM D2487 (Unified Soil Classification System) all the soil mixes can be considered sand since more than 50% passes no. 4 sieve. Although there are slight differences in both D_{50} and C_u of the soil mixes considered, no significant effect of those on the small strain behavior is expected.

Table 2. Average and standard deviation (in parenthesis) of shape parameters of the 3D printed sand mixes

Soil specimen	e_{max}	e_{min}	D_{50}	C_u	C_c
Mix 1	0.732 (0.037)	0.471 (0.016)	3.2	1.00	1.00
Mix 2	0.787 (0.036)	0.490 (0.004)	3.2	1.47	1.02
Mix 3	0.776 (0.008)	0.483 (0.008)	2.5	1.26	0.95
Mix 4	0.825 (0.008)	0.507 (0.006)	3.2	1.47	1.02
Mix 6	0.812 (0.013)	0.499 (0.011)	2.5	1.26	0.95
Mix 7	0.861 (0.012)	0.513 (0.005)	2.5	1.26	0.95
Mix 8	0.849 (0.027)	0.501 (0.009)	2.5	1.26	0.95

All the particles were generated using an *Objet Eden 260V* printer from Stratasys with *VeroWhitePlus* rigid acrylate-based polymer resin with a horizontal printing resolution of 30 μm. As previously shown by Ahmed and Martinez [2020, 2021], the polyjet printer is able to create 3D printed

particles that succesfully reproduce the shape of natural sand particles, as evidenced by the negigible differences in the shape parameters reported in their study. The hardened polymer resin has Young's modulus of 2.4 GPa, Poisson's ratio of 0.3 and specific gravity of 1.18. The polyjet 3D printing process results in a large surface roughness, which is greater than that typical of natural soil particles, as shown in the comparison of X-ray CT scans presented in Figure 3 and further descibed in Ahmed and Martinez [2020, 2021]. Due to the smaller Young's modulus and the greater surface roughness, the stiffness of the interparticle contacts between 3D printed particles is smaller compared to that for natural sands. Figure 4a shows the results of interparticle uniaxial compression tests performed by Ahmed and Martinez [2020] on spherical polyjet particles with diameter of 3.175 mm. The results show that initial increases in force result in a soft contact response due to plastic yielding of the particles' microasperities. As the load is increased, the contact becomes stiffer and follows the Hertzian solution more closely. For comparison, Figure 4b presents similar results for a pair of glass spheres with diameter of 3.175 mm, showing the stiffer contact response that closely follows Hertz solution. Figure 4c shows the results of a single grain crushing test on Leighton Buzzard Sand (LBS) from Cavarretta et al. [2010]. The response of LBS also shows an initial softer response due to plastic yielding of microasperities, followed by a stiffer response that conforms well to Hertz theory.

Another important difference between the polyjet particles and natural sand particles is the magnitude and anisotropy of the friction coefficient of the former. Namely, the friction coefficient measured perpendicular to the printing direction (0.11 to 0.19) was considerably smaller than that measured along the printing direction (0.38 to 0.50) [Ahmed and Martinez, 2021]. The friction coefficients measured perpendicular to the printing direction are also considerably smaller than measurements on natural sand particles, which range between 0.17 and 0.36. The reader is referenced to Ahmed and Martinez [2020, 2021] for a detailed description of the compressive and frictional contact response of polyjet particles.

The roundness and sphericities of the printed particles were obtained from image analysis using the code by Zheng and Hryciw [2015], and the convexity was obtained using the solidity function in Matlab. The particle images were obtained using a white light scanner with a resolution of 0.1 µm (VR-3100, Keyence, Osaka, Japan). The analysis of results also considered three combined shape parameters: regularity (R_G), overall regularity (OR) and shape-angularity group indicator ($SAGI$). Regularity of a particle is the average of R and S_C [Cho et al., 2006], overall regularity is the average of R, S_P, S_{WL} and C [Liu and Yang, 2018] and $SAGI$ is defined by the relationship $SAGI = 5.4(1 - S_{WL}) - 67.8(1 - C) - 77.9(1 - S_P)$ [Altuhafi et al., 2016]. The maximum and minimum void ratios of all the mixes were determined using the methods outlined in Carey et al. [2020], which have been shown to provide maximum and minimum void ratios similar to those provided by the ASTM D4254 and ASTM D4253 methods. The

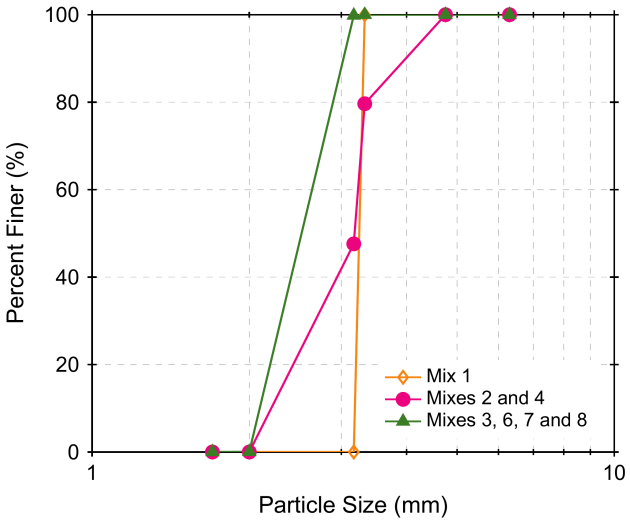

Figure 2. Grain size distribution of all the 3D printed sand mixes

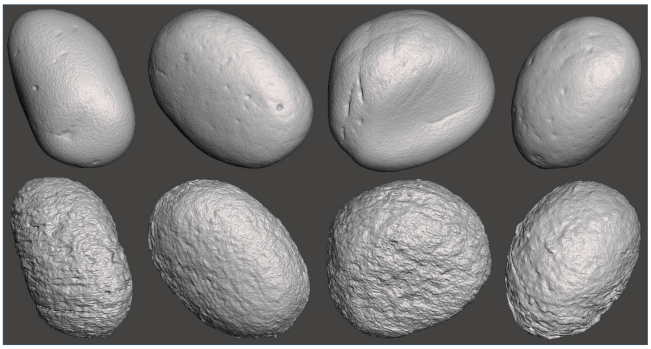

Figure 3. Comparison of X-ray CT scans of natural (top row) and 3D printed particles (bottom row) of mix 2

results are shown in Table 2. Figure 5 shows the variation of e_{max} and e_{min} with particle R, S_P, and R_G. These parameters were selected to allow for comparison with published relationships from Youd [1973] and Cho et al. [2006]. As shown, the measurements indicate a decrease in e_{max} and e_{min} as roundness, circle ratio sphericity and regularity are increased, which is consistent with the trends from literature. For the relationship with R, the e_{max} and e_{min} measurements fall in between the relationships from Youd [1973] and Cho et al. [2006] (Figure 5a); however, the trends reported by Cho et al. [2006] indicate a steeper decrease as S_C and R_G are increased (Figures 5b and 5c). While further research is required to explain these differences, it is possible that the smaller friction coefficient in relation to those reported for natural sands, as presented by Ahmed and Martinez [2021], may result in the smaller void ratio values reported.

2.3. Bender Element Test

Bender element (BE) tests were conducted on specimens with a diameter of 70 mm and a height between 65 and 76 mm contained in a latex membrane of 0.3 mm in thickness. The specimens were prepared inside split molds in five lifts,

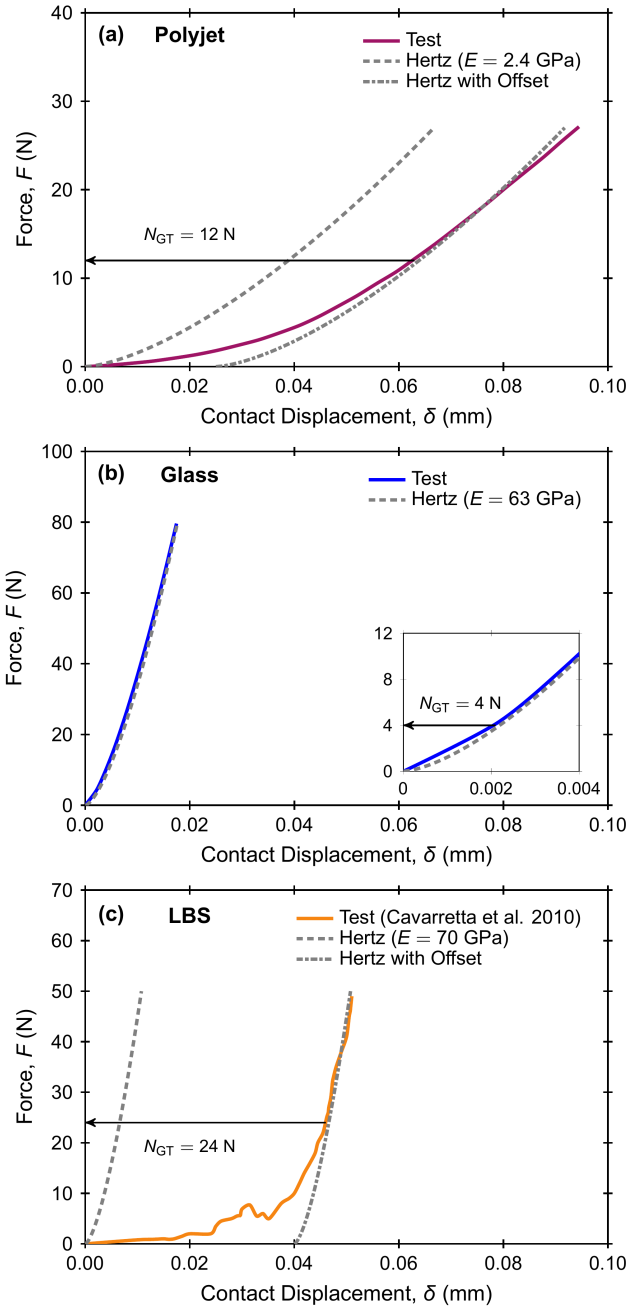

Figure 4. Uniaxial particle-particle compression test results on (a) polyjet 3D printed and (b) glass equal-sized spheres (after Ahmed and Martinez [2020]), and (c) single grain crushing test result on Leighton Buzzard Sand (LBS) after (Cavarretta et al. [2010]). Note: diameter of the spheres is 3.175 mm, and the diameter of the LBS particle is 1.67 mm.

which were poured using a funnel. After pouring of each lift, the mold side was tapped with a rubber mallet to densify the specimen to the target void ratio. Specimens with initial void ratios (e_0) of 0.55 ± 0.02, 0.60 ± 0.02 and 0.65 ± 0.02 were prepared for the seven sand mixes, which corresponded to relative densities (D_R) between 30% and 80%. The BE tests were performed at isotropic confining pressures (p') from 10 to 80 kPa applied by vacuum. However, it is noted that mixes 1, 2, and 4 were tested at p' from 10 to 70 kPa due to a leak in the membrane that developed at greater p' values. BEs attached to the specimen top and bottom caps were used to send and receive S-waves. V_s values were calculated using the travel time of the S-waves and the distance between the BEs. The initial rise of the signal (i.e. the time when a signal first crosses the x-axis) was taken as the wave arrival time [Yamashita et al., 2009]. Ahmed and Martinez [2020] provide further information on the testing setup and results interpretation methodology. Figure 6 shows typical transmitter and receiver BE signals at different p'.

3. Results

3.1. Shear Wave Velocity and Small-Strain Modulus Measurements

The V_s of the specimens composed of all seven materials increased as p' was increased and e_0 was decreased, in agreement with trends for natural soils [e.g. Cho et al., 2006, Hardin and Richart Jr, 1963] as shown in Figures 7a, 7b and 7c for e_0 of 0.55 ± 0.02, 0.60 ± 0.02 and 0.65 ± 0.02, respectively. The V_s for any given p' and e_0 combination increased as the particle roundness and sphericity were increased. For example, the mix with the greatest roundness and sphericity (mix 1) has the greatest V_s whereas the mix with the smallest roundness and sphericity (mix 7) has the smallest V_s. The dependency of V_s on particle shape is discussed in more detail in the following section.

The dependency of V_s on p' can be expressed by the following power-law equation [Lee and Stokoe, 1986]:

$$V_s = \alpha \left(\frac{p'}{1\ \text{kPa}} \right)^{\beta} \tag{6}$$

where α is the shear wave velocity (m/s) at p' of 1 kPa and β reflects the sensitivity to changes in p'. Figure 7 includes power-law fits to the data using Equation 6. As shown, the quality of the fit is high, as evidenced by the high R^2 values. Values of α-coefficients and β-exponents for all the 3D printed sands were obtained from the fitted relationships (Figure 8a). As shown, the α-coefficient generally increased and the β-exponent generally decreased as the e_0 was decreased, in agreement with trends reported by Cha et al. [2014]. The values of the α-coefficients ranged between 90 and 124 m/s whereas the values of the β-exponents ranged between 0.203 and 0.222. The α-coefficient and β-exponent obtained in this study are within the range of those for natural sands (Figure 8b) [Cha et al., 2014]. Analytical relationships for the β-exponents indicate values of 0.167 for a Hertzian contact and of 0.25 for particles experiencing contact yield [Cascante and Santamarina, 1996]. The β-exponents obtained in this investigation are within this range possibly due to local asperity yielding and particle rearrangement caused by the increases in p', as expected for natural sands [Cascante and Santamarina, 1996].

It is noted that the range of β-exponent values reported by Cho et al. [2006] and Cha et al. [2014] range from 0.07 to 0.36, while those from the measurements on the 3D printed sands presented herein ranges from 0.21 to 0.25. While it

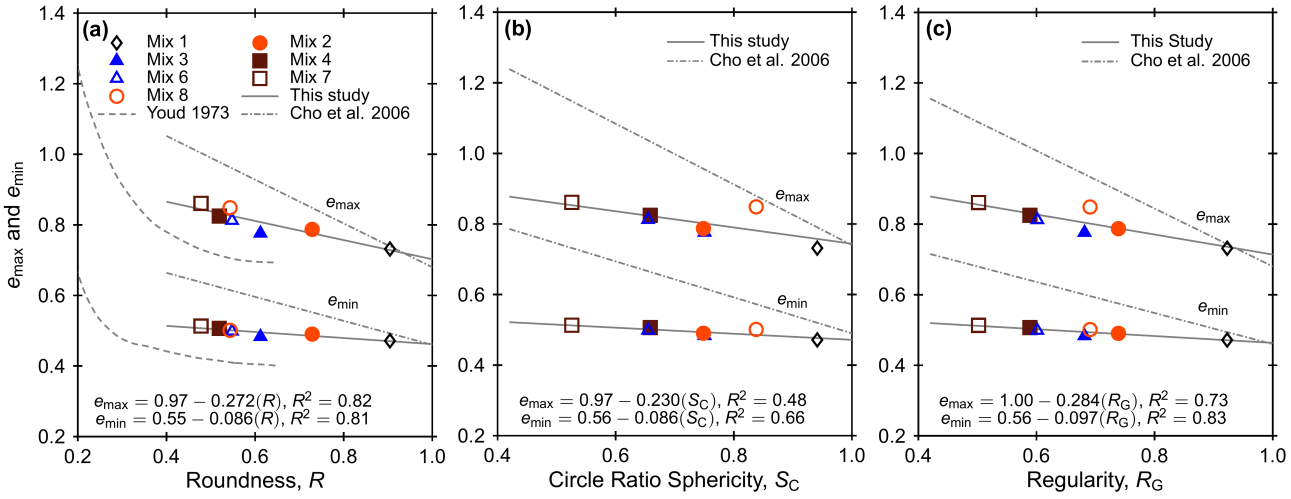

Figure 5. Variation of maximum and minimum void ratios of all the sand mixes with (a) roundness, (b) circle ratio sphericity, and (c) regularity.

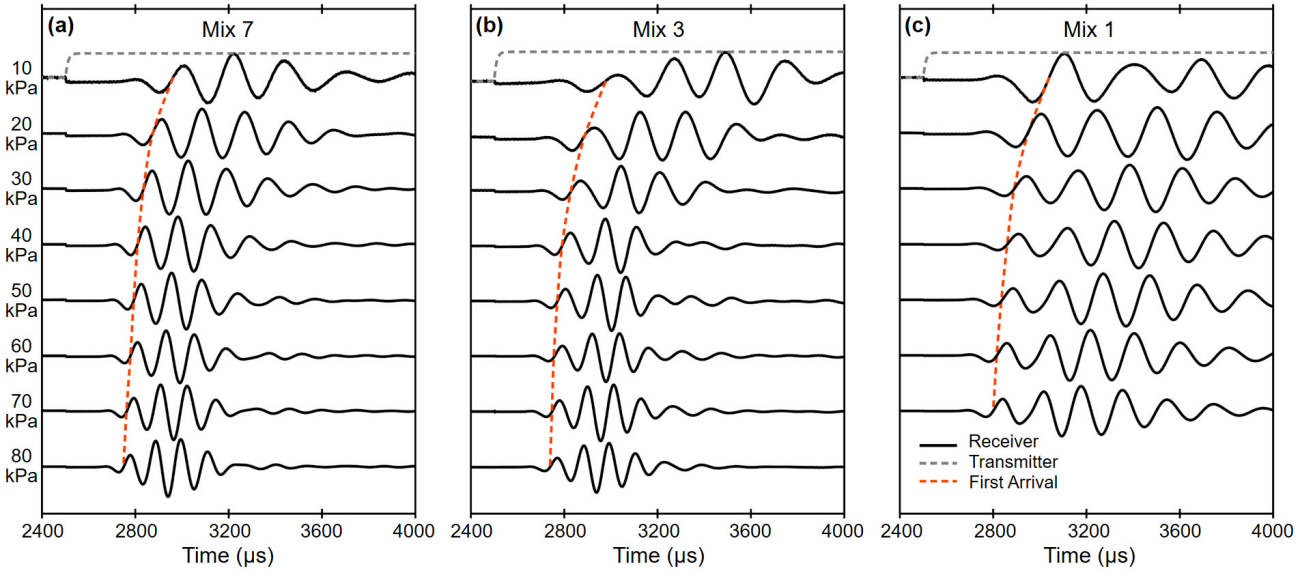

Figure 6. Receiver bender element signals for specimens of (a) mix 7 (initial height of 74.6 mm), (b) mix 3 (initial height of 72.2 mm) and (c) mix 1 (initial height of 67.8 mm) with $e_0 = 0.60 \pm 0.02$.

is possible that that the greater compressibility of the polymeric material is responsible for the smaller range of β values, it is likely that the smaller range is due to the isolation of the particle shape effects from those of particle size and mineralogy. In fact, this is suggested by Ahmed and Martinez [2020], who show a similar range of β-exponents (i.e. 0.20 to 0.23) for rounded and angular natural sands with the same mineralogy and particle size and shape as the values (i.e. 0.20 to 0.25) for 3D printed sands obtained from X-ray CT scans of the natural sands.

Small-strain shear modulus values were calculated using the relation $G_{max} = \rho V_s^2$, where ρ is the specimen total density (Figures 7d, 7e and 7f). It is noted that the G_{max} values reported are smaller than those typical of natural sands due to the smaller specific gravity of the 3D printed sands (1.18 compared to 2.65 to 2.7 for silica sands) and the smaller stiffness of the polymeric constituent material (Young's modulus of 2.4 GPa compared to about 76 GPa for silica sands). The relationship between G_{max} and p' can be represented by the following power-law equation [Hardin and Richart Jr, 1963]:

$$G_{max} = AF(e)\left(\frac{p'}{1\ \text{kPa}}\right)^n \tag{7}$$

where A is a coefficient that depends on the particle arrangement and elastic properties of constituent material, $F(e)$ is the function of e_0 as described by Hardin and Richart Jr [1963], and n describes the sensitivity to changes in p'. Figure 8c shows the A and n values obtained by fitting power functions. As shown, the A-coefficient generally increased and the n-exponent generally decreased as e_0 was decreased. The n-exponents for all the specimens range

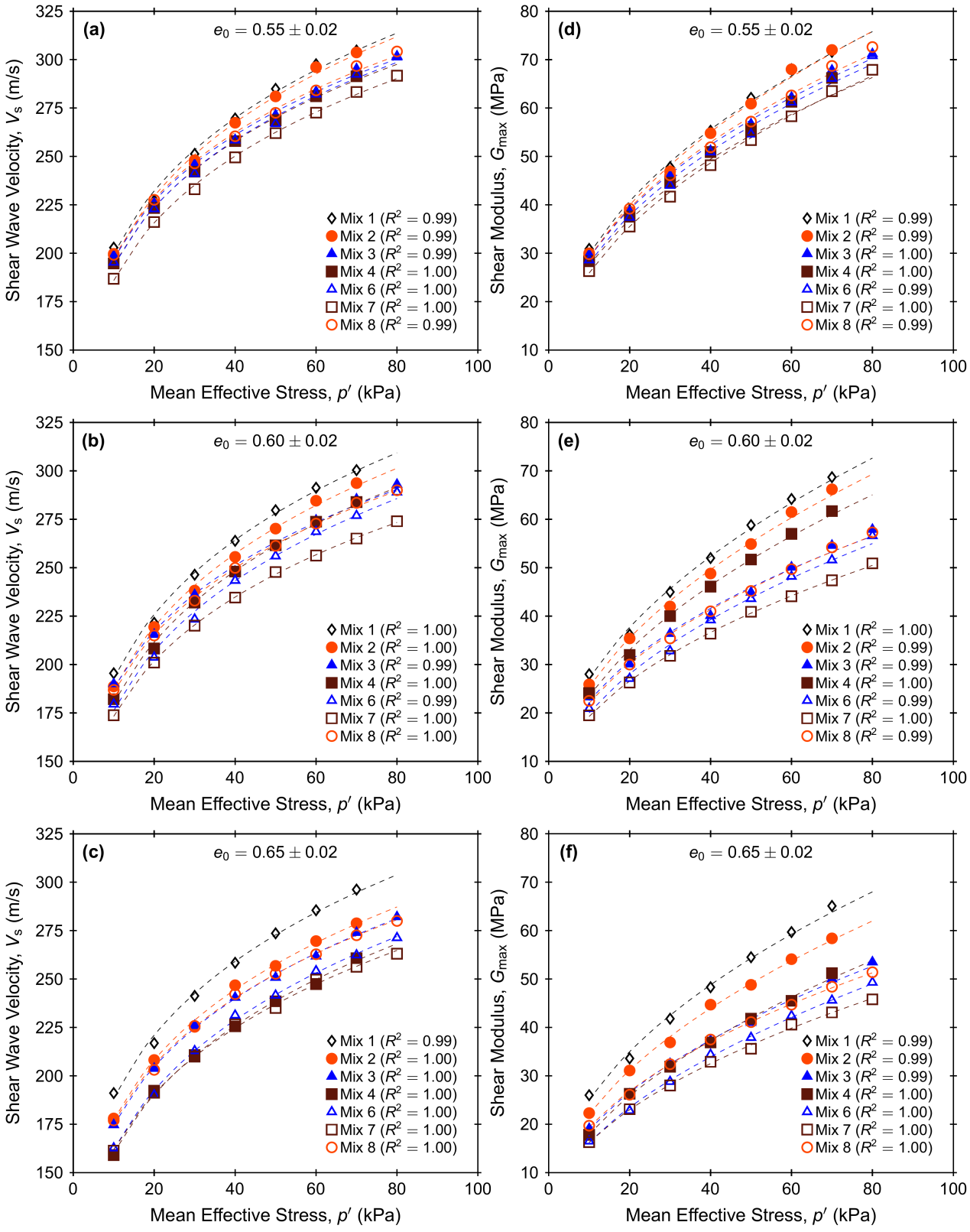

Figure 7. (a, b, c) Shear wave velocities and (d, e, f) shear moduli for all the specimens of 3D printed sands under isotropic confining pressures ranging from 10 to 80 kPa.

between 0.424 and 0.463, which are greater than the value of 0.33 for the Hertz solution, in agreement with those reported in literature [e.g. Chung et al., 1984, Hardin and Black, 1966].

The V_s of the specimens composed of all seven mixes are also evaluated for specimens of similar relative density to account for differences in e_{max} and e_{min} and state, as shown in Figure 9. The results indicate the same trends as previously

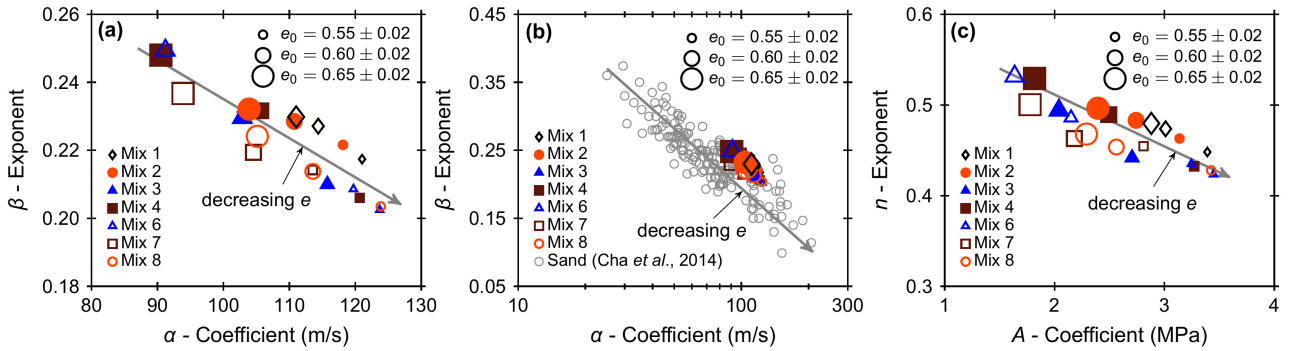

Figure 8. (a) Relationship between β-exponents and α-coefficients for all the specimens of 3D printed sands, (b) comparison of β-exponents and α-coefficients with database of natural sands from Cha et al. [2014] and (c) relationship between n-exponents and A-coefficients for all the specimens of 3D printed sands.

described in Figures 7a, 7b, and 7c. Namely, V_s increased as p' and D_R were increased. For any given combination of p' and D_R , V_s increased as the particle roundness and sphericity were increased.

3.2. Effect of Particle Shape on Shear Wave Velocity and Small-Strain Modulus

The results presented in Figures 7 and 9 allow for examination of the effects of particle shape on V_s for specific combinations of e_0 (or D_R) and p'. Such results are presented in Figure 10 for a p' of 50 kPa and e_0 of 0.55 and 0.65. It is noted that the trends reported here are true for all other combinations of p' and e_0, which are not shown here for brevity. The results show that V_s increases as R (Figures 10a and 10e), S_{WL} (Figures 10b and 10f), S_C (Figures 10c and 10g) and S_P (Figures 10d and 10h) are increased for any given e_0. The correlation with V_s is strongest with the R parameter (R^2 between 0.89 and 0.90), followed by that with S_P and S_C (R^2 between 0.75 and 0.84) and weakest with S_{WL} (R^2 between 0.66 and 0.75). These differences imply that the R parameter is a stronger predictor of V_s, likely because this parameter reflects the radii of the particle asperities which in turn determine the stiffness of the inter-particle contact. This contrasts with the S_P, S_C, and S_{WL} parameters which capture the overall particle shape. Similar trends as reported for V_s were observed for G_{max} (shown in Figure A1 in Appendix), with an increase in G_{max} with increasing shape parameters and a stronger correlation between G_{max} and R. The shear wave velocity results can also be grouped according to their relative density, as shown in Figure A2 in Appendix. The results reveal similar trends, with V_s increasing with increasing R, S_{WL}, S_C and S_P and with increasing D_R for all stress levels.

The effects of particle shape on V_s are further examined using the combined shape parameters R_G, OR and $SAGI$. The results shown in Figure 11 correspond to a p' of 50 kPa. As shown, V_s increases as R_G and OR are increased, and decreases as $SAGI$ is increased, in agreement with the trends in Figure 10. Stronger correlations are observed between V_s and the combined shape parameters (R^2 between 0.90 and 0.98 for R_G, OR and $SAGI$) than between V_s and the individual shape parameters (R^2 between 0.66 and 0.90 for R, S_{WL}, S_C and S_P). These trends likely reflect the complex relationship between contact stiffness (and thus V_s) and different

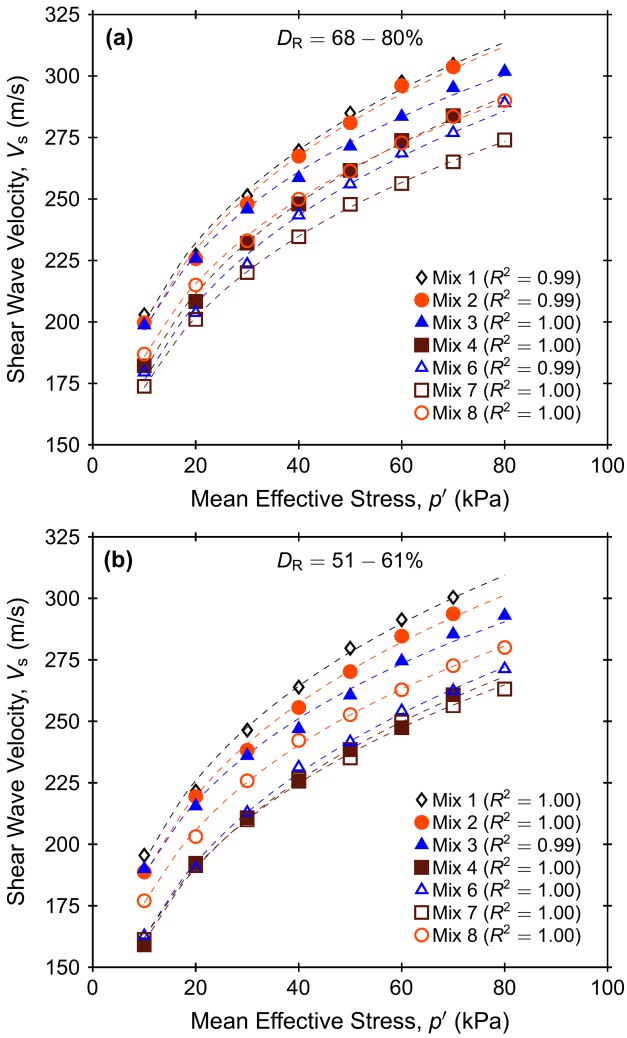

Figure 9. Shear wave velocities for all the specimens of 3D printed sands under isotropic confining pressures ranging from 10 to 80 kPa for (a) D_R = 68-80% and (b) D_R = 51-61%.

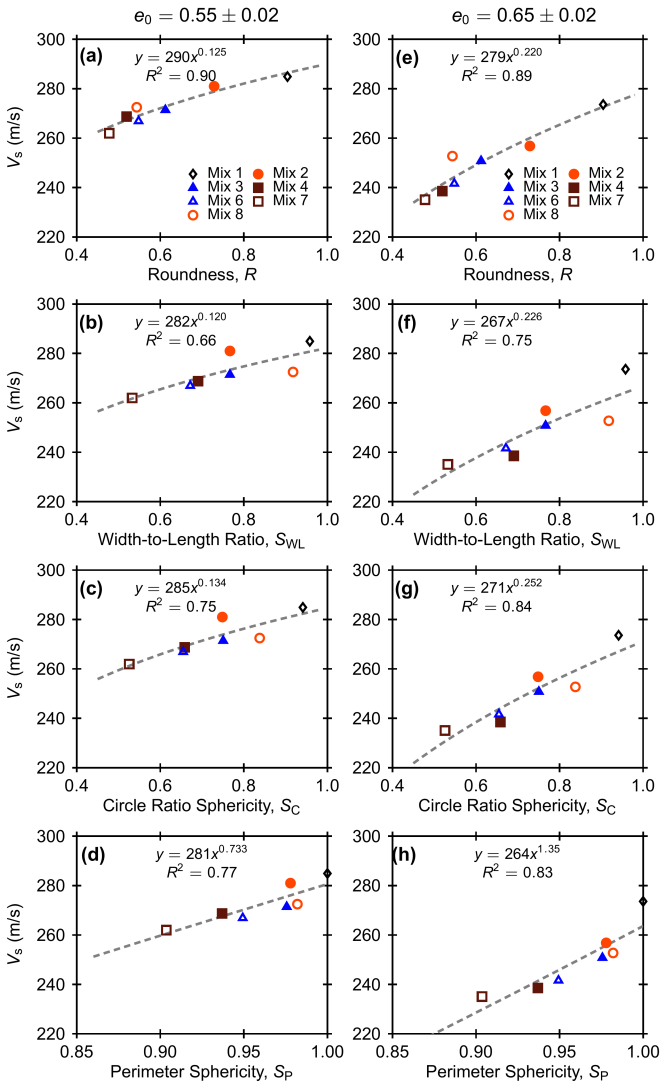

Figure 10. Variation of shear wave velocities with roundness, width-to-length ratio, circle ratio sphericity and perimeter sphericity, respectively for all the specimens at $p' = 50$ kPa with (a, b, c, d) $e_0 = 0.55 \pm 0.02$ and (e, f, g, h) $e_0 = 0.65 \pm 0.02$.

aspects of particle shape; the combined shape parameters seem to better capture this complexity, at least phenomenologically. The G_{max} values show similar trends as described for V_s (shown in Figure A3 in Appendix), consisting of an increase of G_{max} with increases in R_G and OR and decreases in $SAGI$. The trends between V_s and the combined shape parameters are also true for specimens of similar D_R, as shown in Fig. A4 in the Appendix, with R^2 values between 0.81 and 0.95.

The variation of α-coefficient and β-exponent values obtained from power-law fits (Equation 6) with several of the shape parameters are presented in Figures 12a to 12h. As shown, the α-coefficient increased as R, R_G and OR were increased, and decreased as $SAGI$ was increased for any given e_0 (Figures 12a to 12d). This indicates an increase in the contact stiffness at a p' of 1 kPa as R, R_G and OR increase and as $SAGI$ decreases. Additionally, the α-coefficient increased as e_0 was decreased, as expected. Figures 12e, 12f, 12g and 12h indicate no clear trend between the β-exponent and the shape parameters. This suggests that for the 3D printed soils, the shape parameters are poor predictors for β and that β depends only on e_0. Comparison of these trends with published relationships is discussed in the following section. A similar analysis for the A-coefficient and n-exponent for the power-law fits for G_{max} (Equation 7) are presented in Figure A5 in the Appendix. These results indicate similar trends, with increases in A as R, R_G and OR increase and as $SAGI$ decreases, and no clear influence of the shape parameters on n. However, both parameters show dependence on e_0.

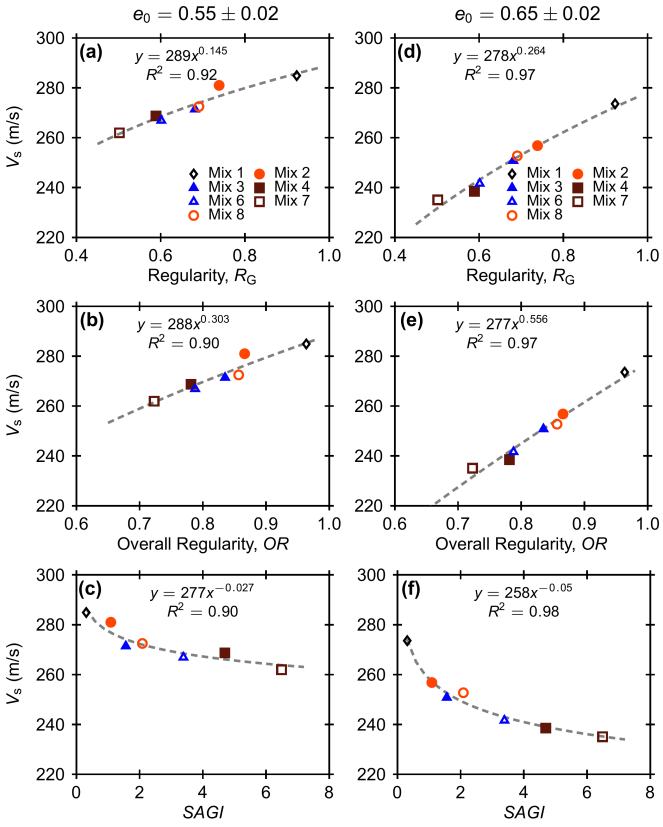

Figure 11. Variation of shear wave velocities with regularity, overall regularity and $SAGI$, respectively for all the specimens at $p' = 50$ kPa with (a, b, c) $e_0 = 0.55 \pm 0.02$ and (d, e, f) $e_0 = 0.65 \pm 0.02$.

Several published studies show an increase in V_s and α and a decrease in β as particle roundness, sphericity, and regularity are increased [Bui, 2009, Cho et al., 2006, Lee et al., 2017, Patel et al., 2009]. However, other studies report a decrease in small-strain stiffness with increases in roundness, sphericity, and regularity [Altuhafi et al., 2016, Liu and Yang, 2018, Liu et al., 2021, Shin and Santamarina, 2013]. A reason that may lead to this disagreement include differences in testing configurations and interpretation methods used to obtain shear wave velocity measurements. Another reason is the intertwined effects of different particle and soil properties and whether these were considered in the aforementioned studies. In particular, the latter may be an important consideration as D_{50}, C_u, e_0, and mineralogy

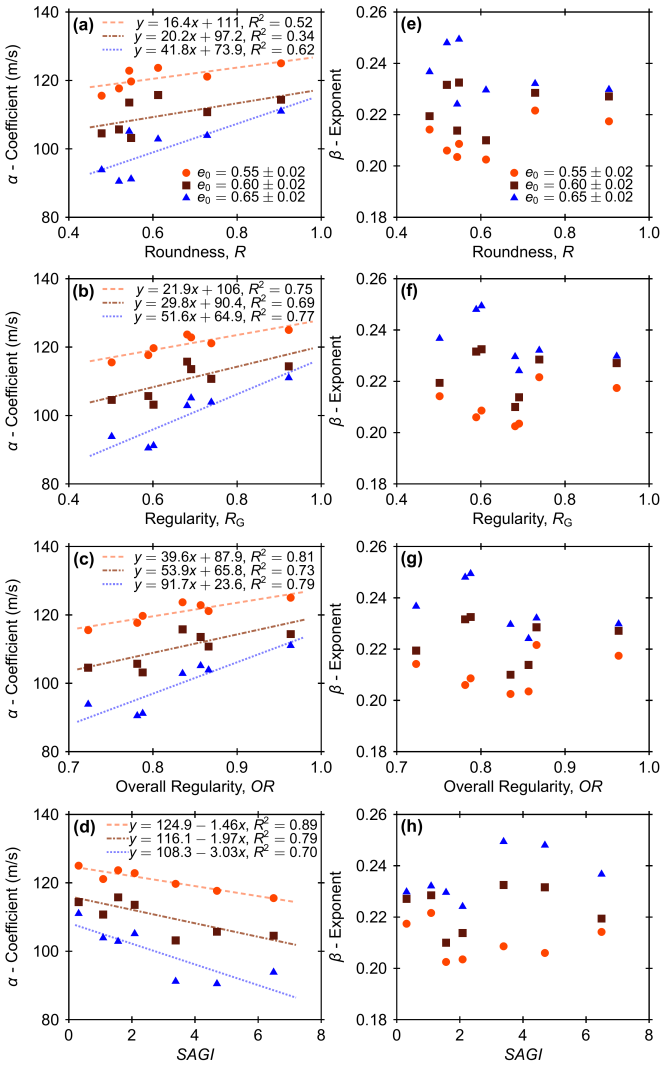

Figure 12. Variation of (a, b, c, d) α-coefficients and (e, f, g, h) β-exponents with roundness, regularity, overall regularity and $SAGI$, respectively, for all the specimens.

have all shown to affect shear wave velocity magnitudes [e.g. Hussien and Karray, 2015, Menq, 2003, Sharifipour et al., 2004]. For example, Cho et al. [2006] does not recognize the effect of e_0 in the V_s, α, and β values. While Altuhafi et al. [2016] found an increase in G_{max} with increasing $SAGI$, the authors also report a weak increase in G_{max} with increasing particle surface roughness (S_q) which in turn is shown to increase with $SAGI$. This is however in contrast with results from analytical solutions and other experimental results, indicating a decrease in G_{max} with increasing S_q [e.g. Otsubo et al., 2015]. Indeed, Liu and Yang [2018] discuss aspects leading to uncertainty in establishing relationships between particle shape parameters and G_{max} associated with the aforementioned interrelationships. These interdependencies among particle shape parameters, their influence on soil void ratio and density, and their aggregated effects on V_s further highlight the usefulness of individually controlling particle properties, as enabled by the 3D printing technology.

4. Discussion

4.1. Relationships Between Shear Wave Velocity and Shape Parameters

The results of bender element tests indicate a dependency of the shear wave velocity on the different particle shape parameters and the initial void ratio. To quantify these interrelationships and to compare to published equations developed based on natural sands, a linear regression analysis was performed to determine empirical relationship between V_s and a given shape parameter and e_0. Here, the R parameter is considered due to its widespread use in literature and the R_G, OR and $SAGI$ parameters are considered due to their stronger correlations with V_s (i.e. Figure 11). It is noted that the regression analysis can also consider D_R instead of e_0; the former would capture the effect of state in relation to the extreme void ratios of a given soil while the latter captures the effects of absolute density and coordination number. In the regression analysis, V_s (m/s) was defined according to Equation 6; it is noted that these relationships differ from those presented in Figures 12a to 12h because they include e_0. Based on the results presented in Figures 12a to 12h, α can be defined in terms of different particle shape parameters and e_0, and β is a function of of e_0 only. α and β are expressed as:

$$\alpha = 26.82(R) - 210.21(e_0) + 219.90 \quad (8)$$

$$\alpha = 34.46(R_G) - 210.21(e_0) + 213.24 \quad (9)$$

$$\alpha = 61.74(OR) - 210.21(e_0) + 185.22 \quad (10)$$

$$\alpha = -2.16(SAGI) - 210.21(e_0) + 242.55 \quad (11)$$

$$\beta = 0.2513(e_0) + 0.0724 \quad (12)$$

The equations reflect linear relationships between α and the different shape parameters and e_0, and a linear relationship between β and e_0. The following discussion is limited to the R and R_G shape parameters due to their widespread use in the literature. Correlations between α and β with R and R_G have been previously published by Cho et al. [2006]; a comparison of these relationships with those provided in Equations 8, 9 and 12 are shown in Figures 13a to 13f. While Cho et al. [2006] did not consider the effect of e_0 on α, nor provided e_0 values for their dataset, the predicted values are generally consistent with one another. Namely, the values predicted by the Cho et al. [2006] equation are smaller than those predicted by Equations 8 and 9 for e_0 of 0.55 and 0.65. If a greater e_0 value of 0.80 is considered, the predictions between the Cho et al. [2006] equation and Equations 8 and 9 are close to one another (Figures 13a and 13b). However, it is noted that this falls outside of the range of e_0 values considered in the experiments on 3D printed sands. Cha et al. [2014] indicated an increase in α with decreases in e_0, which is in agreement with Equations 8 and 9 and the results shown in Figures 12a, 12b, 12c and 12d. While Cha et al. [2014] did not provide an equation between in α and e_0, they suggest so by their relationship between α and the coefficient of compression (C_c), which is known to have a strong dependency on e_0 [Vesić and Clough, 1968].

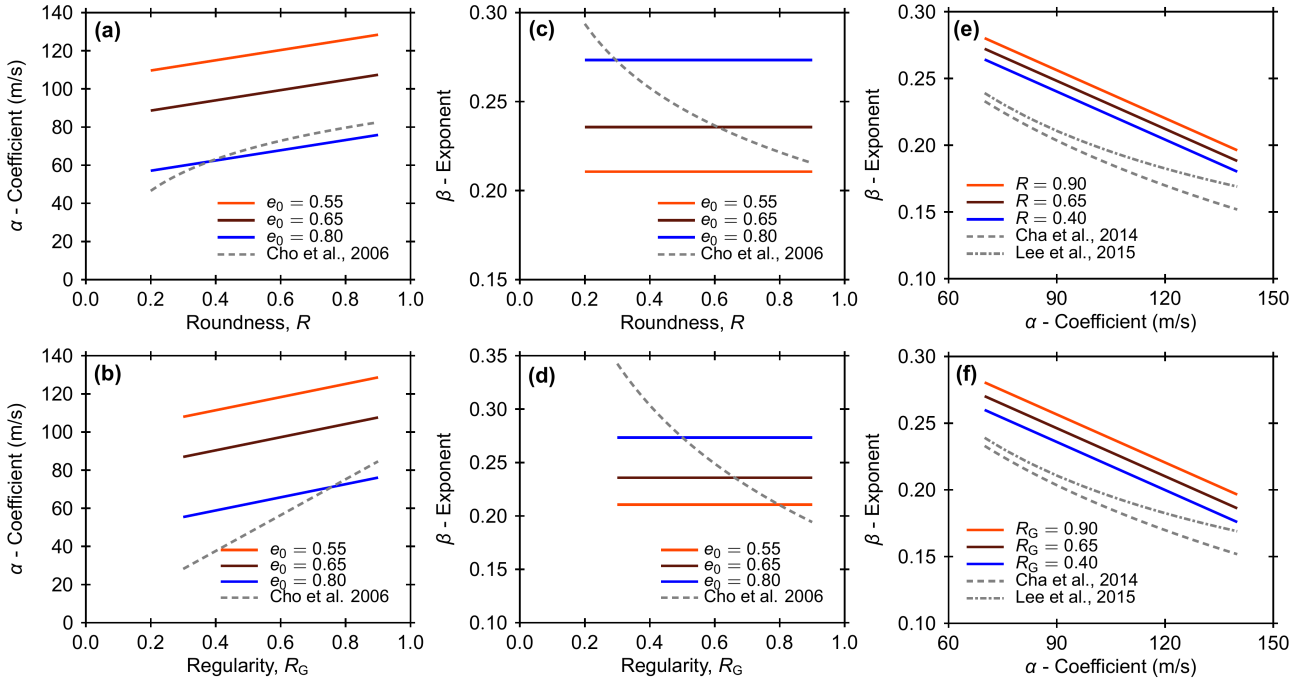

Figure 13. Comparison of (a, b) α-coefficients and (c, d) β-exponents relationships with roundness and regularity, and (e, f) relationships between α-coefficients and β-exponents for different roundness and regularity.

Table 3. Data from literature used for comparison

Sand	R	R_G	e_0	p' (kPa)	References
Blue Sand 1	0.240	0.375	0.69 - 0.84	100	Payan et al. [2016a]
Sydney Sand	0.610	0.685	0.75	50 - 400	Payan et al. [2016b]
Ottawa Sand	0.652		0.60 - 0.70	100 - 500	Liu and Yang [2018]
Fujian A Sand	0.499		0.65 - 0.76	100 - 500	
Fujian B Sand	0.560		0.62 - 0.71	100 - 500	
Toyoura Sand	0.513		0.65 - 0.77	100 - 500	
Material A1		0.44	0.741	100 - 500	Liu et al. [2021]
Material A2		0.44	0.539	100 - 500	
Material B1		0.63	0.813	100 - 500	
Material B2		0.65	0.470	100 - 500	

Cho et al. [2006] also provided an equation between the β-exponent and R and R_G without consideration of the effect of void ratio. However, Cha et al. [2014] report a decrease in β with decreases in void ratio, in agreement with Equation 12. Figures 13c and 13d shows that the values predicted by Equation 12 are within the range of the values predicted by the Cho et al. [2006] equation, with closer agreement at greater void ratios for small roundness values and at smaller void ratios with larger roundness. It is possible that the decrease in attainable e_0 values with increases in R and R_G (i.e. as reported by Youd [1973] and Cho et al. [2006] and shown in Figure 5) causes a concomitant decrease in β-exponent. In fact, Patel et al. [2009] provided an equation for V_s that explicitely considers e_{max} and e_{min} in addition to other particle shape and size parameters.

Equations 8, 9 and 12 can be manipulated to write the following :

$$\beta = 0.032R - 0.0012\alpha + 0.335 \quad (13)$$

$$\beta = 0.041R_G - 0.0012\alpha + 0.327 \quad (14)$$

As shown, the equations are independent of e_0 but dependent on the particle shape parameters. Figures 13e and 13f shows inverse relationship between α and β. The figures also provide the relationships presented by Cha et al. [2014] and Lee et al. [2017]. The predictions based on Equations 8 and 9 are in general agreement with the previously-published relationships, with slightly greater predicted β values likely due to the greater compressibility of the contacts of the 3D printed particles.

To further assess the applicability of Equations 8, 9 and 12 to measurements on natural sands, values predicted using these equations are compared to those reported in the literature (Table 3) in Figure 14. As shown, there is a close agreement between the predicted values and the experimental values reported by the authors, with the bulk of the data falling within the ±15% lines. This agreement, along with the comparisons between Equations 8, 9, 12, 13, and 14 provided in Figure 13, suggests that relationships developed based on tests on 3D printed soils can capture

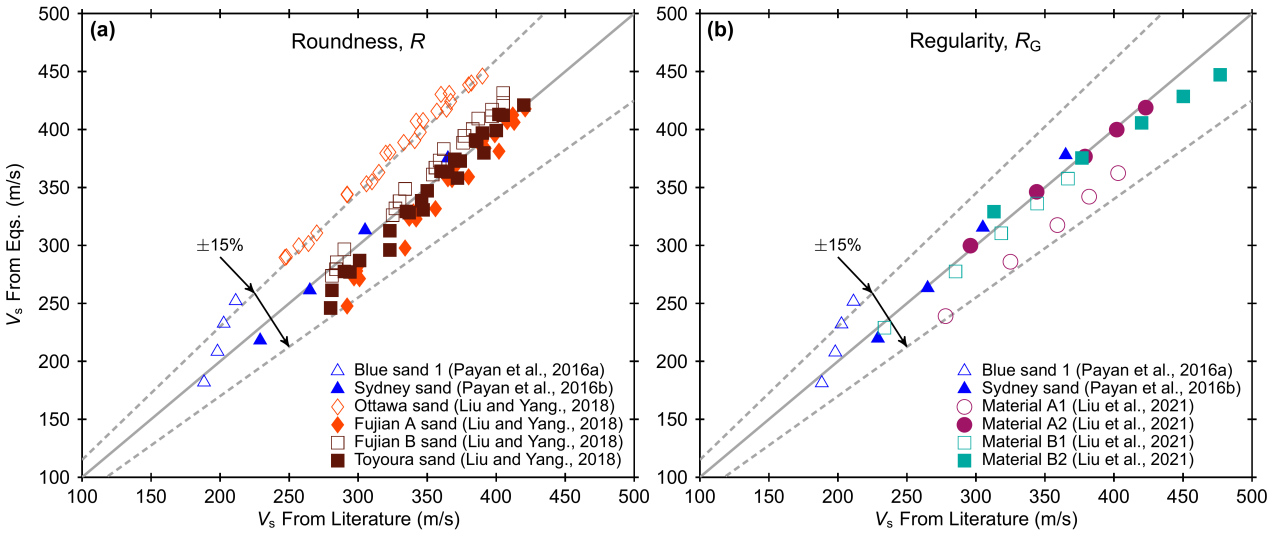

Figure 14. Comparison of shear wave velocities obtained from the regression analysis and literature based on: (a) roundness and (b) regularity.

the effects of particle shape and void ratio on the shear wave velocity of natural sands for the range of mean effective stresses considered in this investigation (i.e. 10 to 80 kPa). This agreement may be unexpected considering the differences in constituent materials between the 3D printed and natural sands. One possible reason for this agreement is that the dependence of V_s on particle shape, void ratio, and effective stress is governed by the particulate nature of soils, which is properly replicated by the 3D printed soils. Another possibility is that while certain parameters or behaviors may have different effects on V_s, these have an aggregated effect that is similar between the 3D printed and natural sands. For example, the effect of the smaller stiffness of the polymeric material could be offset by the effect of the larger interparticle contacts owing to its greater compressibility. Indeed, further research is required to further understand the mechanisms leading to similarities and differences in the behavior of 3D printed and natural soils.

4.2. Considerations on the Modeling of Sand Behavior with 3D Printed Particle Analogs

A significant advantage in using 3D printed soils is the ability to control particle shape while the remaining properties (i.e. particle size, constituent material, surface roughness) are maintained constant, which expand the experimental capabilities available to researchers. A similar procedure can be used to isolate the effects of particle size, as shown by Adamidis et al. [2020]. Despite this benefit, it is important to consider the possible effects of the differences between the 3D printed and natural sands resulting from their different constituent material properties and genesis. Namely, the polymeric material has a smaller stiffness and specific gravity than natural minerals such as quartz. The smaller stiffness of the polymer results in softer interparticle contacts which leads to a greater bulk compressibility, while the smaller density can influence behaviors in which dynamic and inertial effects are important such as tamping and pluviation used for specimen preparation. The layer deposition printing process inherently results in an anisotropic configuration. This has been shown by Ahmed and Martinez [2021] to lead to anisotropy in the interparticle friction coefficient. However, the results presented by Ahmed and Martinez [2020] suggest that the contact normal force-deformation response does not exhibit anisotropy due to the layer deposition orientation. Finally, the printing process can produce a large surface roughness which also leads to softer interparticle contacts. Because different 3D printing technologies (e.g. stereolithography, selective laser sintering, fused deposition moldeling) use different manufacturing processes and are capable of printing different materials, the possible effects of each technology on the response of soil particles should be evaluated and understood. However, it is envisioned that such differences in properties will be addressed as the additive manufacturing technology enables generating objects with a broader suite of materials and processes. Ultimately, comparisons of the measurements on 3D printed analogs with experimental data on natural soils and established relationships can help validate the conclusions drawn from such studies.

5. Conclusion

An investigation on the effects of particle shape on the small-strain behavior of sands using seven 3D printed soils is presented. The synthetic particles were designed based on spherical harmonics and on X-ray CT images from natural sands, allowing for careful control of the materials' particle shape parameters. The same polymeric material and additive manufacturing process was used to generate all the 3D printed materials, thus minimizing the differences in constituent material properties and particle surface roughness. Measurements based on bender element tests indicate an increase in V_s and G_{max} with increasing mean effective stress and decreasing void ratio, in agreement with trends

reported for natural sands. The results also show an increase in V_s and G_{max} with increases in particle roundness, sphericity, and regularity for a given e_0, D_R, and p'.

Fitting the relationship between V_s and p' with a power law (i.e. Eq. 6) shows an increase in the α-coefficient with increases in the particle shape partameters R, S_P, S_C, S_{WL}, R_G, and OR and decreases in $SAGI$, as well as an increase in α with decreases in e_0. In contrast, the β-exponent was found to depend on e_0 but to be independent of the particle shape parameters. The correlations between V_s and the combined shape parameters R_G, OR, and $SAGI$ was shown to be stronger than with the individual shape parameters R, S_P, S_C and S_{WL}, likely because the former parameters better capture the effects of different aspects of particles (i.e. the shape of the corners as well as the overall particle shape). The results of this study are used to develop equations for the α-coefficient and β-exponent that consider their dependency on particle shape and e_0. These equations are shown to agree with published relationships and to predict the V_s values of natural sands with an error ±15%. This close agreement suggests that 3D printed soils can be reliably used to model the small-strain behavior of natural sands. However, it is important to consider differences in the inherent behaviors of 3D printed and natural sands, such as the smaller contact stiffness of the 3D printed soils owing to the smaller Young's modulus of the polymer material.

Conflicts of Interest

The authors declare that there is no conflict of interest. The complete review history is available online.

Acknowledgements

This material is based upon work supported in part by the National Science Foundation (NSF) under award No. 1735732. Any opinions, findings, and conclusions or recommendations expressed in this material are those of the author(s) and do not necessarily reflect those of the NSF.

References

Adamidis, O., Alber, S., and Anastasopoulos, I. (2020). Assessment of three-dimensional printing of granular media for geotechnical applications. *Geotechnical Testing Journal*, 43(3).

Ahmed, S. S. and Martinez, A. (2020). Modeling the mechanical behavior of coarse-grained soil using additive manufactured particle analogs. *Acta Geotechnica*, 15(10):2829–2847.

Ahmed, S. S. and Martinez, A. (2021). Triaxial compression behavior of 3d printed and natural sands. *Granular Matter*, 23(4):1–21.

Altuhafi, F. N., Coop, M. R., and Georgiannou, V. N. (2016). Effect of particle shape on the mechanical behavior of natural sands. *Journal of Geotechnical and Geoenvironmental Engineering*, 142(12):04016071.

Athanassiadis, A. G., Miskin, M. Z., Kaplan, P., Rodenberg, N., Lee, S. H., Merritt, J., Brown, E., Amend, J., Lipson, H., and Jaeger, H. M. (2014). Particle shape effects on the stress response of granular packings. *Soft Matter*, 10(1):48–59.

Bartake, P. and Singh, D. (2007). Studies on the determination of shear wave velocity in sands. *Geomechanics and Geoengineering*, 2(1):41–49.

Braun, P., Tzortzopoulos, G., and Stefanou, I. (2021). Design of sand-based, 3-d-printed analog faults with controlled frictional properties. *Journal of Geophysical Research: Solid Earth*, 126(5):e2020JB020520.

Bui, M. T. (2009). *Influence of some particle characteristics on the small strain response of granular materials.* PhD thesis, University of Southampton.

Carey, T. J., Stone, N., and Kutter, B. L. (2020). Grain size analysis and maximum and minimum dry density testing of ottawa f-65 sand for leap-ucd-2017. In *Model tests and numerical simulations of liquefaction and lateral spreading*, pages 31–44. Springer.

Cascante, G. and Santamarina, J. C. (1996). Interparticle contact behavior and wave propagation. *Journal of Geotechnical Engineering*, 122(10):831–839.

Cavarretta, I., Coop, M., and O'Sullivan, C. (2010). The influence of particle characteristics on the behaviour of coarse grained soils. *Géotechnique*, 60(6):413–423.

Cha, M., Santamarina, J. C., Kim, H.-S., and Cho, G.-C. (2014). Small-strain stiffness, shear-wave velocity, and soil compressibility. *Journal of Geotechnical and Geoenvironmental Engineering*, 140(10):06014011.

Chang, N.-Y. and Ko, H.-Y. (1982). Effects of grain size distribution on dynamic properties and liquefaction potential of granular soils. Research Report R82-103, University of Colorado at Denver.

Cho, G.-C., Dodds, J., and Santamarina, J. C. (2006). Particle shape effects on packing density, stiffness, and strength: Natural and crushed sands. *Journal of Geotechnical and Geoenvironmental Engineering*, 132(5):591–602.

Chung, R. M., Yokel, F. Y., and Drnevich, V. (1984). Evaluation of dynamic properties of sands by resonant column testing. *Geotechnical Testing Journal*, 7(2):60–69.

Dutta, T., Otsubo, M., Kuwano, R., and O'Sullivan, C. (2020). Evolution of shear wave velocity during triaxial compression. *Soils and Foundations*, 60(6):1357–1370.

Guida, G., Viggiani, G. M., and Casini, F. (2020). Multi-scale morphological descriptors from the fractal analysis of particle contour. *Acta Geotechnica*, 15(5):1067–1080.

Hafez, A., Liu, Q., Finkbeiner, T., Alouhali, R. A., Moellendick, T. E., and Santamarina, J. C. (2021). The effect of particle shape on discharge and clogging. *Scientific Reports*, 11(1):1–11.

Hanaor, D., Gan, Y., Revay, M., Airey, D., and Einav, I. (2016). 3d printable geomaterials. *Géotechnique*, 66(4):323–332.

Hardin, B. O. and Black, W. L. (1966). Sand stiffness under various triaxial stresses. *Journal of the Soil Mechanics and Foundations Division*, 92(2):27–42.

Hardin, B. O. and Richart Jr, F. (1963). Elastic wave velocities in granular soils. *Journal of the Soil Mechanics and Foundations Division*, 89(1):33–65.

Hussien, M. N. and Karray, M. (2015). Shear wave velocity as a geotechnical parameter: an overview. *Canadian Geotechnical Journal*, 53(2):252–272.

Iwasaki, T. and Tatsuoka, F. (1977). Effects of grain size and grading on dynamic shear moduli of sands. *Soils and Foundations*, 17(3):19–35.

Jiménez, M., Romero, L., Domínguez, I. A., Espinosa, M. d. M., and Domínguez, M. (2019). Additive manufacturing technologies: an overview about 3d printing methods and future prospects. *Complexity*, 2019.

Kirkpatrick, W. (1965). Effects of grain size and grading on the shearing behaviour of granular materials. In *Proceedings of the sixth International Conference on Soil Mechanics and Foundation Engineering*, pages 273–277.

Kittu, A., Watters, M., Cavarretta, I., and Bernhardt-Barry, M. (2019). Characterization of additive manufactured particles for dem validation studies. *Granular Matter*, 21(3):1–15.

Lee, C., Suh, H. S., Yoon, B., and Yun, T. S. (2017). Particle shape effect on thermal conductivity and shear wave velocity in sands. *Acta Geotechnica*, 12(3):615–625.

Lee, S. and Stokoe, K. (1986). Investigation of low-amplitude shear wave velocity in anisotropic material. Geotechnical Engineering Report GR86-6, The University of Texas at Austin.

Li, Y., Zhou, H., Liu, H., Ding, X., and Zhang, W. (2021). Geotechnical properties of 3d-printed transparent granular soil. *Acta Geotechnica*, 16(6):1789–1800.

Liu, X. and Yang, J. (2018). Shear wave velocity in sand: effect of grain shape. *Géotechnique*, 68(8):742–748.

Liu, X., Zou, D., Liu, J., Zheng, B., Zhou, C., and Bai, J. (2021). A gradation-dependent particle shape factor for characterizing small-strain shear modulus of sand-gravel mixtures. *Transportation Geotechnics*, 28:100548.

Marschi, N. D., Chan, C. K., and Seed, H. B. (1972). Evaluation of properties of rockfill materials. *Journal of the Soil Mechanics and Foundations Division*, 98(1):95–114.

Matsumura, S., Kobayashi, T., Mizutani, T., and Bathurst, R. J. (2017). Manufacture of bonded granular soil using x-ray ct scanning and 3d printing. *Geotechnical Testing Journal*, 40(6):1000–1010.

Menq, F.-Y. (2003). *Dynamic properties of sandy and gravelly soils*. PhD thesis, The University of Texas at Austin.

Miskin, M. Z. and Jaeger, H. M. (2013). Adapting granular materials through artificial evolution. *Nature Materials*, 12(4):326–331.

Mitchell, J. K., Soga, K., et al. (2005). *Fundamentals of soil behavior*. John Wiley & Sons New York.

Najmon, J. C., Raeisi, S., and Tovar, A. (2019). Review of additive manufacturing technologies and applications in the aerospace industry. *Additive Manufacturing for the Aerospace Industry*, pages 7–31.

Ngo, T. D., Kashani, A., Imbalzano, G., Nguyen, K. T., and Hui, D. (2018). Additive manufacturing (3d printing): A review of materials, methods, applications and challenges. *Composites Part B: Engineering*, 143:172–196.

Otsubo, M., O'sullivan, C., Sim, W. W., and Ibraim, E. (2015). Quantitative assessment of the influence of surface roughness on soil stiffness. *Géotechnique*, 65(8):694–700.

Patel, A., Bartake, P., and Singh, D. (2009). An empirical relationship for determining shear wave velocity in granular materials accounting for grain morphology. *Geotechnical Testing Journal*, 32(1):1–10.

Payan, M., Khoshghalb, A., Senetakis, K., and Khalili, N. (2016a). Effect of particle shape and validity of gmax models for sand: A critical review and a new expression. *Computers and Geotechnics*, 72:28–41.

Payan, M., Khoshghalb, A., Senetakis, K., and Khalili, N. (2016b). Small-strain stiffness of sand subjected to stress anisotropy. *Soil Dynamics and Earthquake Engineering*, 88:143–151.

Peerun, M., Ong, D. E. L., Desha, C., Oh, E., and Choo, C. S. (2021). Advances in the study of micromechanical behaviour for granular materials using micro-ct scanner and 3d printing. In *International Conference of the International Association for Computer Methods and Advances in Geomechanics*, pages 911–918. Springer.

Santamarina, J. C. (2003). Soil behavior at the microscale: particle forces. In *Soil behavior and soft ground construction*, pages 25–56.

Senetakis, K., Anastasiadis, A., and Pitilakis, K. (2012). The small-strain shear modulus and damping ratio of quartz and volcanic sands. *Geotechnical Testing Journal*, 35(6):964–980.

Sharifipour, M., Dano, C., and Hicher, P.-Y. (2004). Wave velocities in assemblies of glass beads using bender-extender elements. In *17th ASCE Engineering Mechanics Conference*.

Shin, H. and Santamarina, J. C. (2013). Role of particle angularity on the mechanical behavior of granular mixtures. *Journal of Geotechnical and Geoenvironmental Engineering*, 139(2):353–355.

Su, Y. F., Lee, S. J., and Sukumaran, B. (2020). Influence of particle morphology simplification on the simulation of granular material behavior. *Granular Matter*, 22(1):1–12.

Vangla, P. and Latha, G. M. (2015). Influence of particle size on the friction and interfacial shear strength of sands of similar morphology. *International Journal of Geosynthetics and Ground Engineering*, 1(1):6.

Vesić, A. S. and Clough, G. W. (1968). Behavior of granular materials under high stresses. *Journal of the Soil Mechanics and Foundations Division*, 94(3):661–688.

Wadell, H. (1932). Volume, shape, and roundness of rock particles. *The Journal of Geology*, 40(5):443–451.

Wang, J.-J., Zhang, H.-P., Tang, S.-C., and Liang, Y. (2013). Effects of particle size distribution on shear strength of accumulation soil. *Journal of Geotechnical and Geoenvironmental Engineering*, 139(11):1994–1997.

Wei, D., Wang, J., and Zhao, B. (2018). A simple method for particle shape generation with spherical harmonics. *Powder Technology*, 330:284–291.

Wei, D., Wang, Z., Pereira, J.-M., and Gan, Y. (2021). Permeability of uniformly graded 3d printed granular media. *Geophysical Research Letters*, 48(5).

Wichtmann, T. and Triantafyllidis, T. (2009). Influence of the grain-size distribution curve of quartz sand on the small strain shear modulus g max. *Journal of Geotechnical and Geoenvironmental Engineering*, 135(10):1404–1418.

Xiao, Y., Long, L., Matthew Evans, T., Zhou, H., Liu, H., and Stuedlein, A. W. (2019). Effect of particle shape on

stress-dilatancy responses of medium-dense sands. *Journal of Geotechnical and Geoenvironmental Engineering*, 145(2):04018105.

Yamashita, S., Kawaguchi, T., Nakata, Y., Mikami, T., Fujiwara, T., and Shibuya, S. (2009). Interpretation of international parallel test on the measurement of gmax using bender elements. *Soils and Foundations*, 49(4):631–650.

Yang, J. and Gu, X. (2013). Shear stiffness of granular material at small strains: does it depend on grain size? *Géotechnique*, 63(2):165–179.

Youd, T. (1973). Factors controlling maximum and minimum densities of sands. In *Evaluation of Relative Density and its Role in Geotechnical Projects Involving Cohesionless Soils*, pages 98–112. ASTM International.

Zheng, J. and Hryciw, R. D. (2015). Traditional soil particle sphericity, roundness and surface roughness by computational geometry. *Géotechnique*, 65(6):494–506.

Appendix

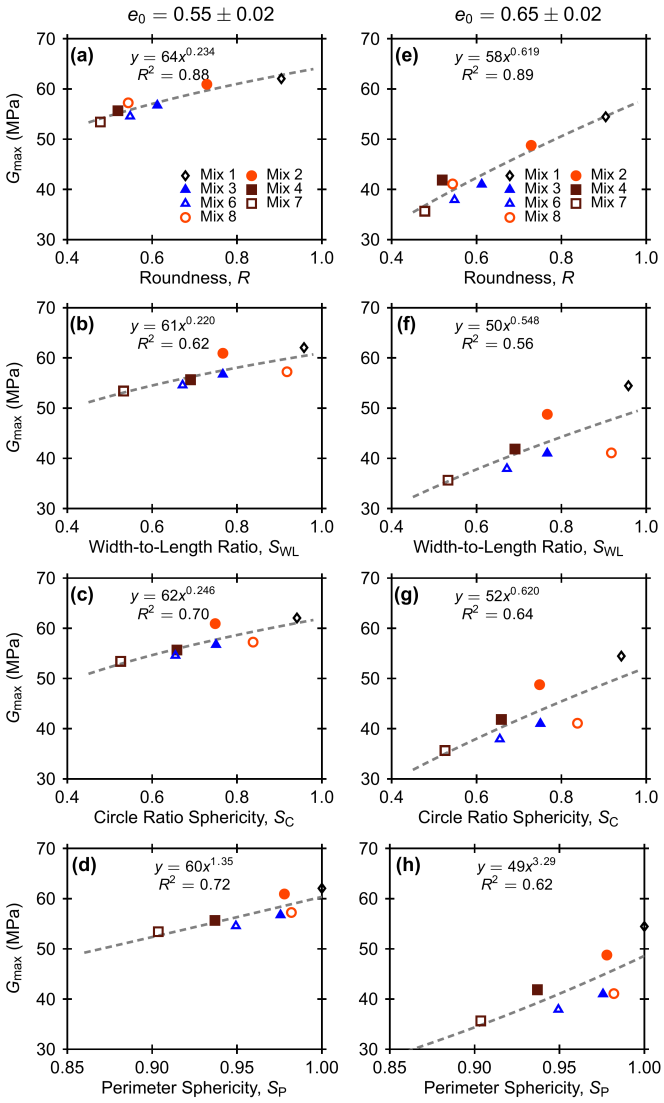

Figure A1. Variation of shear moduli with roundness, width-to-length ratio, circle ratio sphericity and perimeter sphericity, respectively, for all the specimens at p' = 50 kPa with (a, b, c, d) $e_0 = 0.55 \pm 0.02$ and (e, f, g, h) $e_0 = 0.65 \pm 0.02$.

Manuscript received 28th July 2021, revised 3rd February 2022, accepted 21st February 2022.

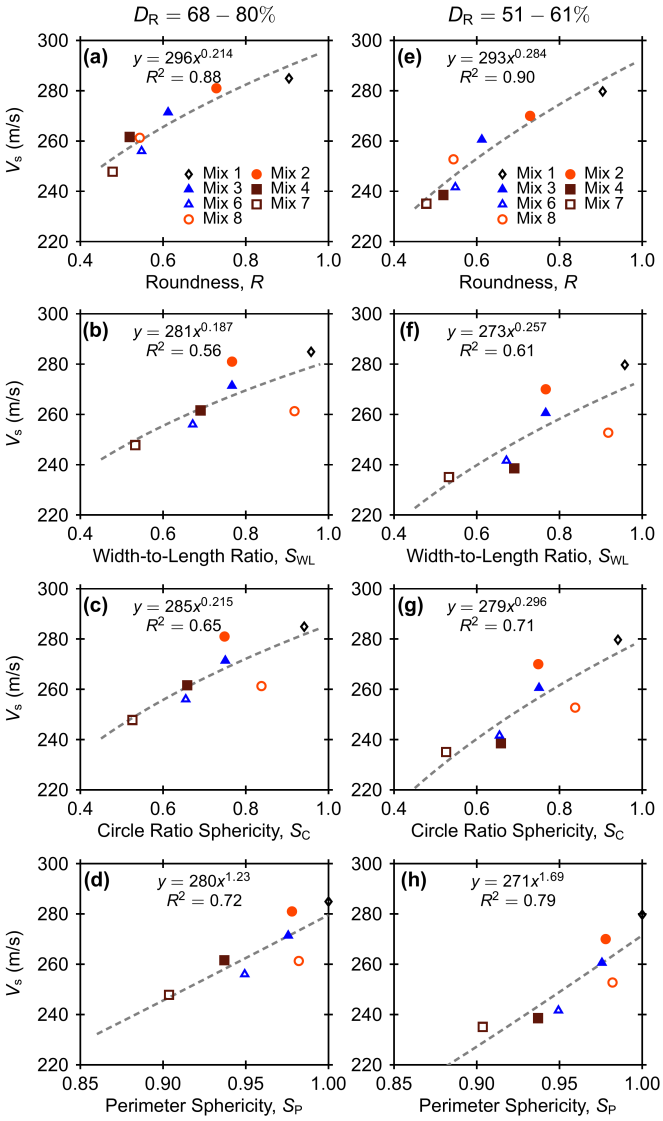

Figure A2. Variation of shear wave velocities with roundness, width-to-length ratio, circle ratio sphericity and perimeter sphericity, respectively, for all the specimens at $p' = 50$ kPa with (a, b, c, d) $D_R = 68$-80% and (e, f, g, h) $D_R = 51$-61%.

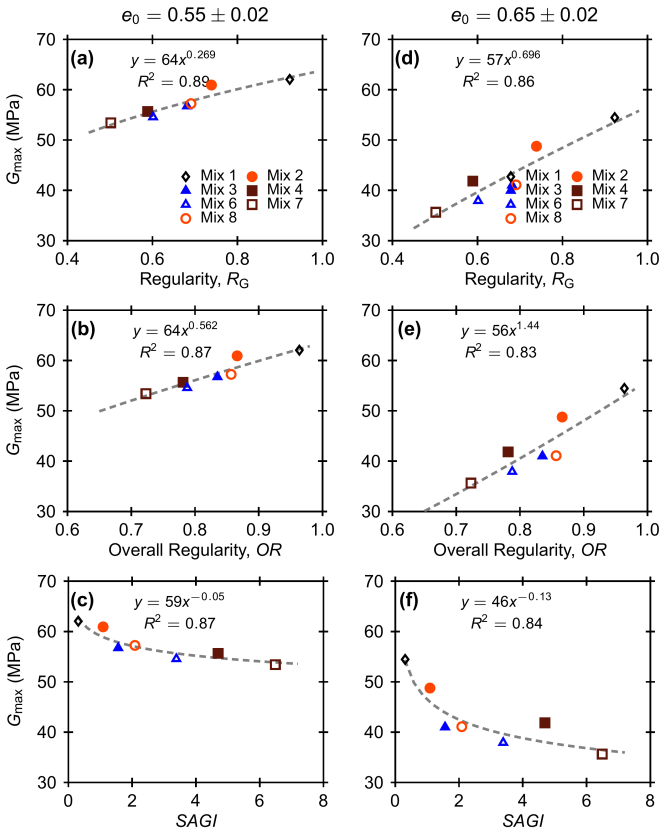

Figure A3. Variation of shear moduli with regularity, overall regularity and $SAGI$, respectively, for all the specimens at $p' = 50$ kPa with (a, b, c) $e_0 = 0.55 \pm 0.02$ and (d, e, f) $e_0 = 0.65 \pm 0.02$.

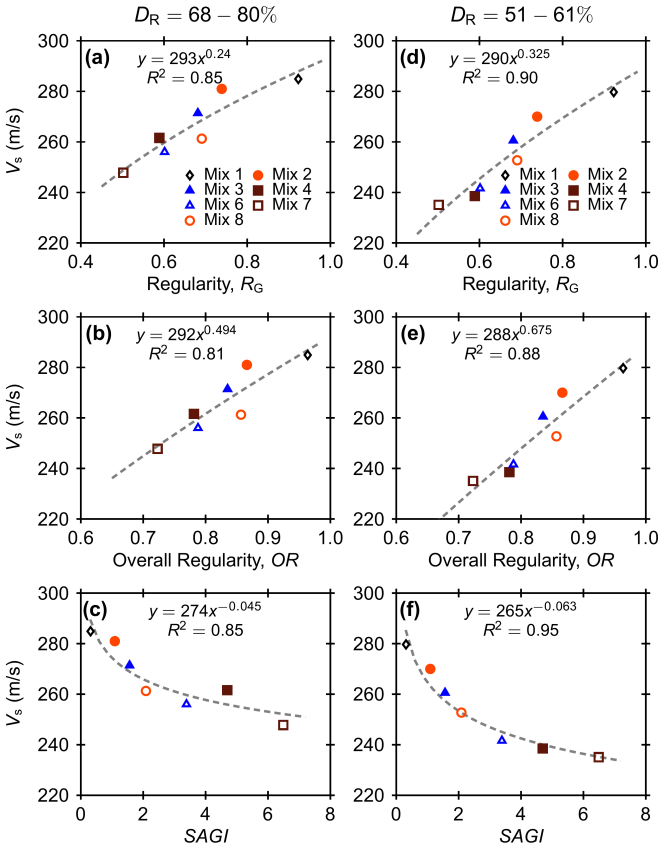

Figure A4. Variation of shear wave velocities with regularity, overall regularity and SAGI, respectively for all the specimens at p' = 50 kPa with (a, b, c) D_R = 68-80% and (d, e, f) D_R = 51-61%.

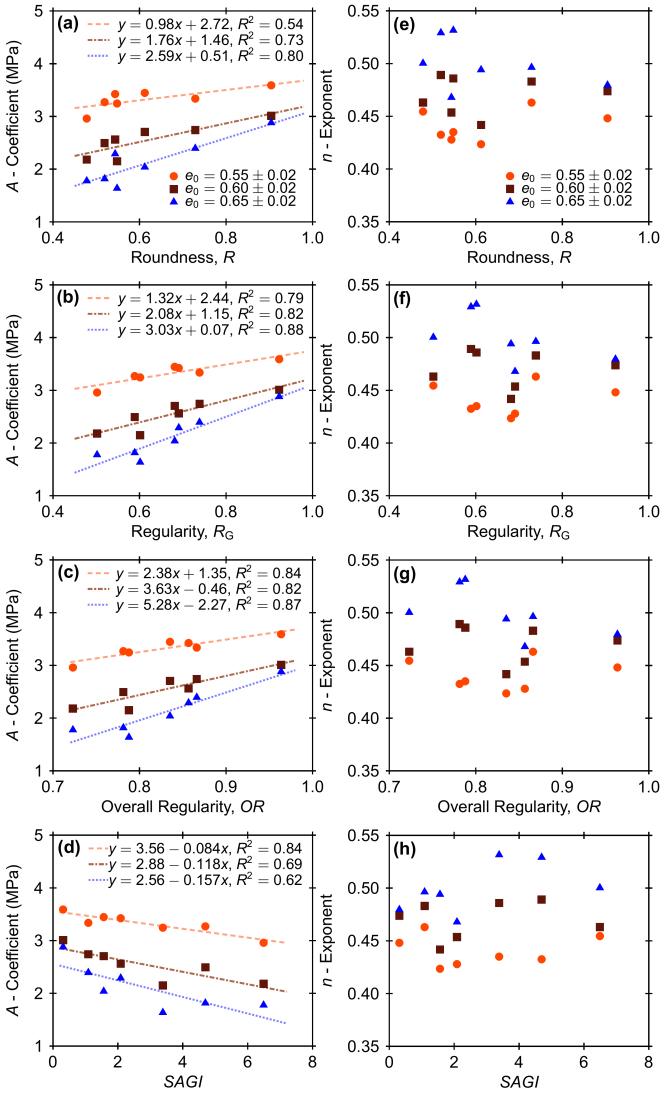

Figure A5. Variation of (a, b, c) A-coefficients and (d, e, f) n-exponents with regularity, overall regularity and $SAGI$, respectively, for all the specimens.